# Mechanical properties and microstructural evaluation of the heat-affected zone in ultra-high strength steels

Amraei Mohsen, Afkhami Shahriar, Javaheri Vahid, Larkiola Jari, Skriko Tuomas, Björk Timo, Zhao Xiao-Ling



**DOI:** 10.1016/j.tws.2020.107072

Contents lists available at ScienceDirect

Thin-Walled Structures

journal homepage: http://ees.elsevier.com

# Mechanical properties and microstructural evaluation of the heat-affected zone in ultra-high strength steels

Mohsen Amraei [a,b], Shahriar Afkhami [b], Vahid Javaheri [c], Jari Larkiola [c], Tuomas Skriko [d], Timo Björk [b], Xiao-Ling Zhao [a,*]

[a] The School of Civil and Environmental Engineering, UNSW Sydney, NSW, 2052, Australia
[b] Laboratory of Steel Structures, LUT University, P.O. Box 20, 53851, Lappeenranta, Finland
[c] Materials and Mechanical Engineering, University of Oulu, 90014, Finland
[d] Laboratory of Welding Technology, LUT University, P.O. Box 20, 53851, Lappeenranta, Finland

ARTICLE INFO

*Keywords*
Ultra-high strength steel
Welding
Heat affected zone
Mechanical properties
Microstructure

ABSTRACT

This paper presents an investigation into the mechanical properties of ultra-high strength steels (UHSSs) (with nominal yield stress of 960 and 1100 MPa) after welding. Seven weld thermal cycles were simulated using a Gleeble 3800 thermal-mechanical machine. These cycles represented the temperature-time history of the joint at various distances from the weld fusion line (FL) in a typical gas metal arc welding (GMAW) process. The mechanical properties such as Vickers surface hardness, uniaxial tensile behavior and Charpy impact toughness were examined. Microstructural evaluation using field emission scanning electron microscopy (FESEM) was also conducted. According to the results, the S960 which was a direct-quenched type of steel, showed a considerable reduction in its hardness and tensile strength up to 29 and 32%, respectively. On the other hand, the S1100 which was manufactured via quenched and tempered process, showed only a minor degree of softening at far distances from the weld FL (up to 4%) followed by 2% tensile strength reduction, and hardening close to the FL (up to 13%). Microstructure analysis has been carried out to provide insight to the change of mechanical properties in UHSS after welding.

## 1. Introduction

Ultra-high strength steel (UHSS) usually refers to steel with a nominal yield stress greater than 690 MPa. Using UHSS in structural engineering can lead to savings in engineering work, energy, labor and transport costs since thinner steel sections will be used in construction. Extensive research has been reported in the literature on thin walled steel structures with yield stress not greater than 690 MPa (e.g. Bjorhovde 2004, Zhao et al., 2014, Ban and Shi 2018, Li and Young 2018, Han et al., 2018, Herion et al., 2019, Liu et al., 2018, Chiew et al., 2019) [1–8]. The research on UHSS for structural engineering application has attracted attention of many researchers (e.g. Javidan et al., Nassirnia et al., Farahi et al.) [9–11].

However, there are three major factors limiting their applications i.e. UHSSs are more prone to ductility and toughness problems [12], stability issues due to the thin walled thicknesses [13], and the issues related to weld heat affected zone (HAZ) [14]. Materials engineering sector is contentiously developing UHSS with fine microstructure and balanced mechanical properties [12,15,16]. The developments in fabricating welded UHSS tube and beam helps to overcome stability issues [17,18]. Structural engineers are also developing hybrid thin-walled UHSS/mild or high strength steel tubular forms that has higher load carrying capacity and ductility [19,20]. However, in most of the cases, welding process is implemented to join components due to its ease, cost effectiveness and integrity to the structure. Various welding methods are executed to join UHSS plate and tubes i.e.: gas metal arc welding (GMAW) [21,22], laser welding (LW) [23–25], laser gas-metal-arc hybrid welding [26], and tungsten inert gas welding [27]. The main issues related to these weldments were cold cracking [28], reduction in the joint's strength [29], ductility [24], and fracture toughness [30–32].

Since welding process exposes UHSS to high amount of concentrated heat input (HI) energy, it creates a series of steels at vicinity of the joint [29]. These steels experience different peak temperature and cooling rate based on their distance from the weld fusion line (FL), which are considered as the key parameters affecting microstructure

* Corresponding author.
*E-mail address:* xiaolin.zhao@unsw.edu.au (X-L Zhao)

https://doi.org/10.1016/j.tws.2020.107072
Received 13 May 2020; Received in revised form 15 July 2020; Accepted 11 August 2020
Available online xxx
0263-8231/

and mechanical properties of the joint [33]. The most critical region is the weld HAZ which itself comprises four zones [34]: coarse grain (CG), fine grain (FG), inter-critical (IC), and sub-critical (SC). According to the literature, hardness profile of welded UHSS shows a softening at the SCHAZ in the range of 6–60% [23,29,35]. Since the through-thickness material properties at the welded region vary, the correlation between micro-hardness and the mechanical properties (i.e. yield and ultimate strength) is not valid [29]. Hence, the mechanical properties of each zone are not fully understood, and the available knowledge is limited to the overall behavior of the joint.

This paper is dedicated to the determination of mechanical properties and its correlation to the microstructure of the weld HAZ in UHSSs. For this aim, the thermal cycles of a weld HAZ at various distances from the FL were simulated using a Gleeble 3800 thermal-mechanical simulator machine [36]. The associated thermal cycles represent a gas metal arc welding (GMAW) process with nominal HI value of 0.70 kJ/mm which is one of the commonly used methods to fabricate UHSSs [24]. The replicated specimens were then evaluated by Vickers hardness measurement, quasi-static tensile test and Charpy impact toughness. Microstructure of the specimens is also evaluated using optical microscopy. Two steel grades were considered in this research, S960 and S1100, with the former manufactured via direct quenching (DQ), and the latter via quenching and tempering (Q&T) processes. Even though the two steels are of different grades categorized based on their minimum guaranteed 0.2% proof stress by the manufacturer, they often show nearly similar ultimate strength [29]. Hence, the comparison between the mechanical properties of the weld HAZs in these two steel grades can be connected to their manufacturing history.

The overall objective of this research is to understand the effects of welding thermal cycles on the mechanical properties of the weld HAZ in UHSS. This paper provides a valuable insight to the weld HAZ in thin UHSS plates by correlating the Vickers hardness with 0.2% proof stress, ultimate strength and impact toughness of these two steels. The microstructure evaluation in this paper is elaborated to the knowledge of structural engineering community.

## 2. Experimental procedures

First, the as-received 8 mm plates of S960 and S1100 steel grades were cut and machined to 55 × 10 × 5 mm dimension. Second, thermal cycles related to different locations in heat affected zone were simulated using Gleeble 3800 thermomechanical simulator machine. Third, microhardness evaluation was conducted to make sure that the manufactured specimens represent properties of an actual joint at the HAZ of the studied steels. Fourth, the specimens were machined to flat dog-bone shape and tensile testing was performed. Fifth, Charpy impact toughness at ambient temperature was carried out. Sixth, microstructure of the specimens was evaluated using field emission scanning electron microscope (FESEM) equipped with electron back-scatter diffraction (EBSD).

### 2.1. Materials

Table 1 shows the nominal chemical composition, and mechanical properties of the as-received base materials (BM) according to the manufacturer certificates. The microstructure of the BM of both alloys are a mixture of Bainite and Martensite [29].

### 2.2. Thermal cycle simulation using Gleeble 3800

In order to replicate each sub-zone of the HAZ in a GMAW process, the thermal cycles at seven distances from the weld FL were determined by HAZ-CYCLE module in SmartWeld program [37,38]. SmartWeld is an open-source software developed by Sandia National Laboratories for welding and HAZ modeling. The welding parameters in Amraei et al. [29] were adopted in this study as shown in Table 2. The governed thermal cycles are presented in Fig. 1.

Next, seven samples were cut off from S960 and S1100 plates along to their rolling direction. Then, the samples were machined to match the dimensional requirement of the fixtures mounted on the Gleeble machine. The final dimension of the specimens was 55 × 10 × 5 mm. Each specimen was then undergone the associated thermal cycle in Fig. 1.

After producing the simulated sub-zones, they were labelled according to their steel substrate and their distance from the weld FL (1–7, nearest to furthest, respectively). For example, S960-1 represents the specimen made from S960 steel undergone the cycle No. 1 closest to the FL. A description of each simulated sub-zone is presented in Table 3.

### 2.3. Microhardness evaluation

The cross-section of specimens was machined, grinded and polished in five stages. First, the width of specimens was machined for 3 mm in order to collect the hardness points close to the position in which thermocouples were attached to the specimens. This helps to make sure the measured mechanical properties (and later microstructural analysis) correspond to the heating/cooling cycles as cooling rate might have been different at the near surfaces. Second, grinding was performed for 4 min using abrasive particles with roughness of 120 μm. Third, another 4 min of grinding was conducted using diamond particles with roughness of 9 μm. Fourth, polishing was performed for 6 min using particles with roughness of 3 μm. Fifth, the specimen was etched using 5% Nital solution for 15 s. After, Vickers micro-indentation hardness was performed on polished specimens using a 5 kgf and dwell period of 10 s.

The hardness points were collected along three horizontal lines at the through-thickness of specimens with intervals of 0.5 mm. Two lines were at 1 mm distance to each free surface (upper and lower), and one line was located at the mid-section. For simplicity, they are named as top, bottom and middle, respectively. The hardness profiles are compared to that of a butt-welded GMAW manufactured using the same steels and welding heat input value of 0.7 kJ/mm as shown in section 3. The details of the welding process can be found at [29].

### 2.4. Tensile testing

The specimens were machined using liquid coolant to dog-bone shape as shown in Fig. 2(a). Since the material is not consistent at the

**Table 1**
The nominal chemical composition and mechanical properties of the BMs (wt. %).

| Steel | C | Si | Mn | P | S | V | Cu | Cr | Ni | Mo | CEV |
|---|---|---|---|---|---|---|---|---|---|---|---|
| S960 | 0.088 | 0.04 | 1.13 | 0.010 | 0.000 | 0.009 | 0.011 | 1.00 | 0.05 | 0.117 | 0.59 |
| S1100 | 0.133 | 0.192 | 1.49 | 0.006 | 0.001 | 0.152 | 0.437 | 1.34 | 0.998 | 0.388 | 0.85 |
| | **Hardness (Hv)** | | | **$f_{(0.2\%)}$ (min MPa)** | | | **$f_u$ (MPa)** | | | **$A_5$ (min %)** | |
| S960 | 358 | | | 960 | | | 980–1250 | | | 7 | |
| S1100 | 385 | | | 1100 | | | 1130–1350 | | | 10 | |

**Table 2**
Welding parameters used in the GMAW.

| Parameter | Welding Potential (V) | Welding current (A) | Welding speed (mm/s) | HI (KJ/mm) |
|---|---|---|---|---|
| Value | 25 | 220 | 6.2 | 0.7 |

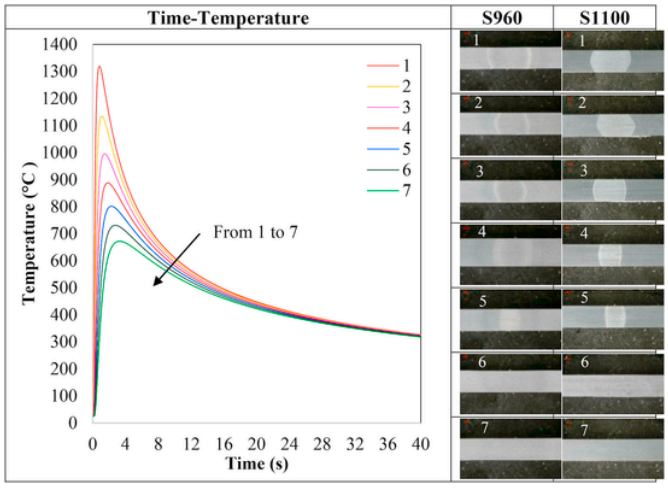


**Fig. 1.** The thermal cycles used in the Gleeble simulator, and the corresponding polished specimens.

**Table 3**
The simulated heating cycles by Gleeble 3800.

| Sub-zone (specimen) | Distance from weld FL (mm) | Approx. peak temperature (°C) | Approx. $\Delta t_{8/5}$ (s) |
|---|---|---|---|
| 1 | 0.0 | 1350 | 10.3 |
| 2 | 0.5 | 1154 | 10.4 |
| 3 | 1.0 | 1000 | 10.5 |
| 4 | 1.5 | 890 | 10.7 |
| 5 | 2.0 | 800 | 11.56 |
| 6 | 2.5 | 730 | – |
| 7 | 3.0 | 670 | – |

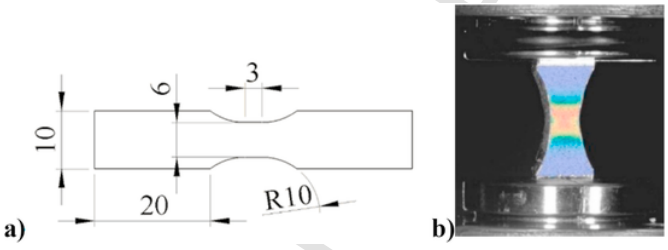


**Fig. 2.** Tensile testing the simulated specimens **a)** machined flat dog-bone shape with gauge length of 3 mm, **b)** distribution of strains captured by the DIC system during tensile testing. (Unit in mm, not to scale).

middle of specimen, the gauge length should be as narrow as possible to keep the failure at the desired area. Otherwise, the failure would occur at the softest region, and similar mechanical properties would govern for all specimens. In order to overcome this challenge and find out where the soft regions are located, the hardness profiles were closely analyzed. It was observed that by keeping the gauge length at 3 mm, it is possible to make sure that the mechanical properties are consistent at the neck area, and specimens would fail from the desired region.

Quasi-static tensile tests were carried out in ambient temperature using a 150 kN Instron machine. The strain rate of the test was at kept constant at $5 \times 10^{-4}$ $s^{-1}$. Strain measurement and its distribution on the surface of specimens was carried out using a full field digital image correlation (DIC) system. The angle between the two cameras of the DIC system, their distance, and working distance from the specimen was set at 25°, 142 mm and 410 mm, respectively.

### 2.5. Charpy impact toughness

Charpy (notch toughness) impact test was carried out on sub-size specimens due to the limited thickness of the raw steel plates. The specimens were prepared following the Annex A3 of the standard ASTM E23 [39]. First, the samples were processed by Gleeble 3800 to impose the welding thermal cycle at the middle of their longitudinal section. Then, a notch was introduced to each sample by mechanical machining. The notch tip was positioned exactly on the simulated sub-zone (in the middle of the sample), as shown in Fig. 3. Finally, the prepared specimens were tested at room temperature.

## 3. Mechanical properties

The hardness evaluation curves are presented in Fig. 4. As can be seen, a reasonable agreement between the simulated specimens and actual weldments has been achieved. All the three measured points (at the top, mid-section and bottom) showed that the through-thickness properties of the replicated HAZ specimens were homogeneous. Hence, it was made sure that the mechanical properties (i.e. tensile and Charpy impact toughness) represent the actual characteristics of each sub-zone.

The S960 revealed 29% reduction in the magnitude of its Vickers hardness at the ICHAZ, while the maximum reduction for S1100 was only 4%. Besides, the two steels showed different softening/hardening behavior at their HAZs. Due to the softened HAZ, the S960 lost a great portion of its surface hardness which agreed with previous reports [14,24]. Yet, due to the low HI and rather high cooling rate of the GMAW process implemented in this study, the hardness reduction was kept below 30%. According to Jiao et al. (2015), reduction in the hardness can reach as high as 60% [40].

On the other hand, the S1100 alloy showed a hardening behavior at its HAZ which was reflected in specimens 1–4. The maximum measured

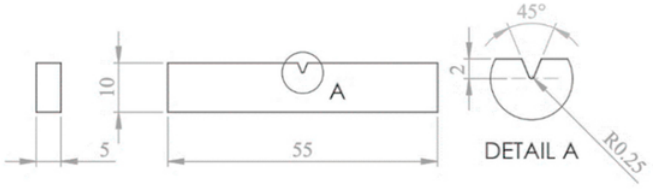


**Fig. 3.** Schematic of the Charpy impact specimen and the notch detail. (Unit in mm, not to scale).

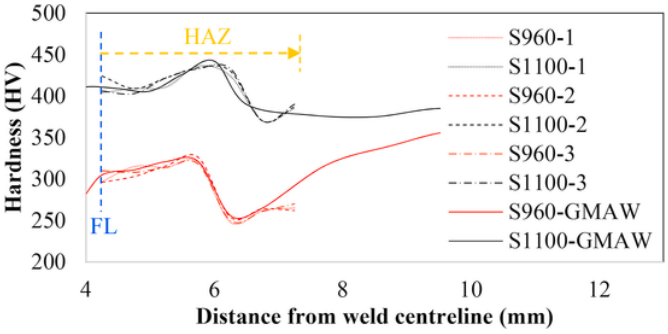


**Fig. 4.** Hardness evaluation results at top, mid-section and bottom of through thickness, labelled as 1, 2 and 3, respectively.

hardness belonged to the weld thermal cycle No. 4 which was 13% higher compared with the S1100 BM. Similar hardening behavior at the HAZ of S1100 is reported by Amraei et al. [29], regardless of the weld HI value.

Similarly, the softened HAZ can be distinguished from tensile test results of the S960 alloy as shown in Fig. 5(a) and (c)). All the simulated S960 specimens showed reduction in both 0.2% proof stress and tensile strength. However, those close to the FL (No. 1–3), in which they experienced the highest peak temperature under the weld thermal cycle, achieved the highest strength compared to other regions. Specimens No. 5 and 6 had the lowest 0.2% proof stress and tensile strength, respectively as shown in Table 4. It is notable that even though the replicated specimens showed a considerable reduction in tensile strength of every zone, the overall strength of the joint was higher. The reason for the higher joint strength compared to the softened HAZ was the boundary condition effect created by the surrounding BM [16].

On the other hand, the S1100 alloy showed much more stability in its tensile properties at various locations from the weld FL as shown in Fig. 5 and Table 5. The 0.2% proof stress in all simulated sub-zones met the specifications of S1100 steel grade as minimum 1100 MPa was achieved. Moreover, the maximum reduction in the tensile strength belonged to specimen No. 6 which was only 2% lower than the BM. Nonetheless, specimens No. 1–5 had considerable higher tensile strength compared with the BM. In an actual weldment, such as the GMAW in this study, the high tensile strength at the vicinity of the softened HAZ creates a rigid boundary in which prevents the tensile stress to accumulate in loading direction. Considering the low degree of softening such as in specimen No. 6 and the strong boundary condition surrounding it, the joint strength at the HAZ rises above that of the BM [29]. Hence, S1100 weldment failed from the BM far from the welded joint. This result contradicts with the other available UHSS grades in which failure occurs at the HAZ followed by considerable reduction in strength and ductility [14,24]. The engineering stress-strain curves of the softest and hardest sub-zones of each steel alloy, and their BM is presented in Fig. 5(c).

The ductility of specimens was evaluated using the strain at ultimate stress divided by the strain at 0.2% proof stress ($\varepsilon_u/\varepsilon_{(0.2\%)}$) as presented in Tables 4 and 5 In general, for the S960 steel alloy studied in this paper, the ductility of all regions increased compared to the BM except for specimen No. 1 which remained almost intact. The soft regions of No. 5 and 6 showed the highest ductility. It is notable that the absolute strain values measured in this paper may not represent the actual values. This is evident when the strain values are compared with a standard test specimen such as $BM_{STD}$ presented in Table 4. The reason was due to the small gauge length and the formation of a notch like stress concentration.

For S1100 steel alloy, ductility of specimens No. 1, 2 and 5 was lower than the BM. Specimen No. 4 which had the highest tensile strength revealed the highest ductility. Yet, the absolute values were much smaller than that of a S1100 BM specimen with standard specimen size. According to Amraei et al. [29], the $\varepsilon_u/\varepsilon_{(0.2\%)}$ of standard tensile test specimens made of the same steel material was 6.14 which

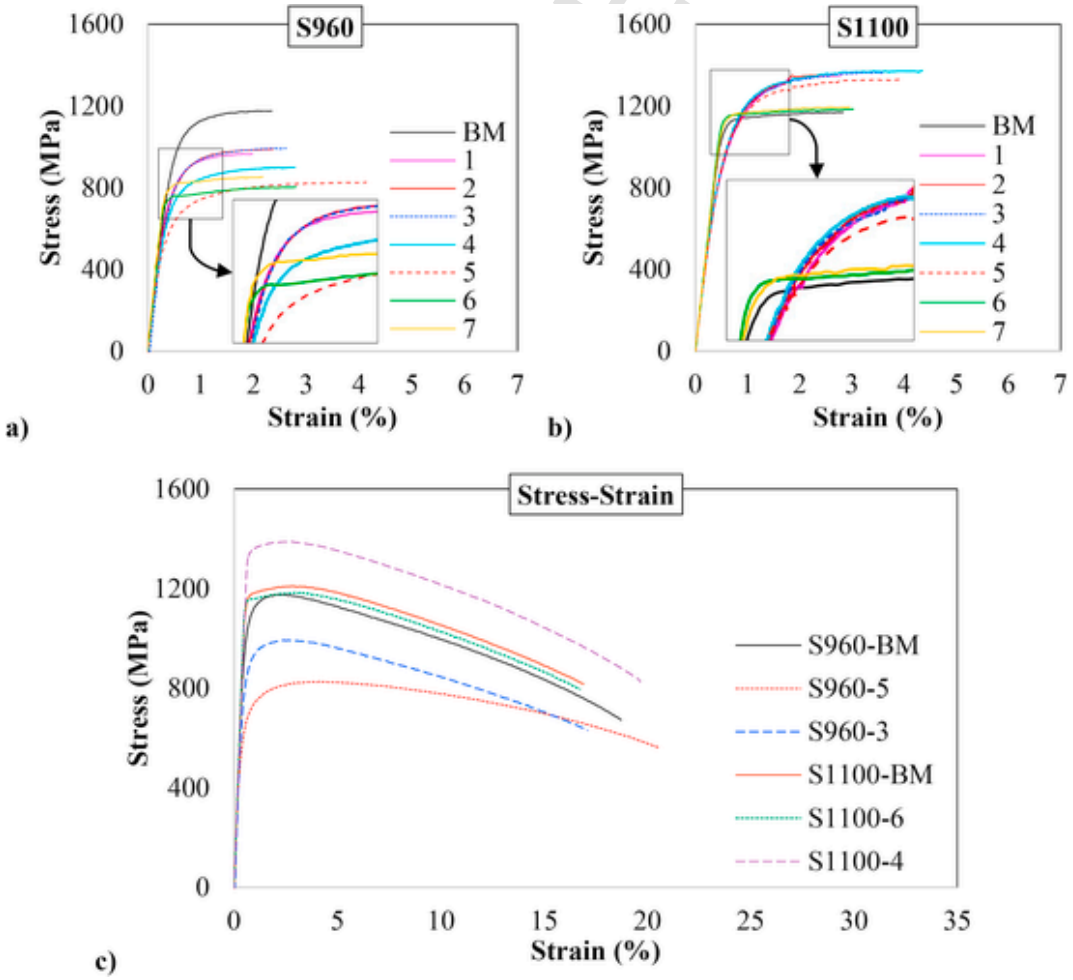


**Fig. 5.** Engineering stress-strain curves of **a)** S960, **b)** S1100, and **c)** comparison between softened and hardened zones. (The curves in "a" and "b" are plotted up to the strain at ultimate stress).

**Table 4**
Mechanical properties of S960 specimens.

| S960 | BM | 1 | 2 | 3 | 4 | 5 | 6 | 7 | $BM_{STD}$* | GMAW [29] |
|---|---|---|---|---|---|---|---|---|---|---|
| $f_{(0.2\%)}$ (MPa) | 1064 | 856 | 851 | 877 | 774 | 667 | 761 | 817 | 989 | 922 |
| $f_u$ (MPa) | 1176 | 967 | 989 | 993 | 900 | 827 | 804 | 854 | 1152 | 1008 |
| $\varepsilon_{(0.2\%)}$ (%) | 0.72 | 0.62 | 0.63 | 0.69 | 0.62 | 0.59 | 0.51 | 0.51 | 0.62 | 0.61 |
| $\varepsilon_u$ (%) | 2.35 | 1.98 | 2.37 | 2.61 | 2.71 | 4.14 | 2.80 | 2.18 | 2.65 | 1.12 |
| $f_u/f_{(0.2\%)}$ | 1.11 | 1.13 | 1.16 | 1.13 | 1.16 | 1.24 | 1.06 | 1.04 | 1.16 | 1.09 |
| $\varepsilon_u/\varepsilon_{(0.2\%)}$ | 3.26 | 3.18 | 3.78 | 3.79 | 4.38 | 6.98 | 5.46 | 4.28 | 4.27 | 1.84 |
| Hardness (Hv) | 358 | 296 | 303 | 316 | 326 | 254 | 264 | 262 | 358 | 221 |
| $f_y$ P&V (MPa) | 939 | 761 | 781 | 818 | 847 | 640 | 669 | 663 | 939 | 545 |
| [a]$f_y$ (MPa) | 1007 | 857 | 874 | 905 | 930 | 754 | 779 | 774 | 1007 | 674 |
| $f_u$ P&V (MPa) | 1237 | 1005 | 1032 | 1080 | 1117 | 849 | 886 | 879 | 1237 | 725 |
| $f_u$ M (MPa) | 1146 | 947 | 970 | 1011 | 1043 | 813 | 845 | 838 | 1146 | 707 |
| [a]$f_u$ (MPa) | 1143 | 949 | 971 | 1012 | 1043 | 818 | 849 | 843 | | 714 |
| Charpy (J) | - | 178 | 190 | 216 | 220 | 166 | 194 | 194 | – | – |

*Refers to a standard size tensile test specimen.
[a] According to the current paper (Eqs. (4) & 5).

**Table 5**
Mechanical properties of S1100 specimens.

| S1100 | BM | 1 | 2 | 3 | 4 | 5 | 6 | 7 | $BM_{STD}$* | GMAW [29] |
|---|---|---|---|---|---|---|---|---|---|---|
| $f_{(0.2\%)}$ (MPa) | 1165 | 1104 | 1119 | 1122 | 1141 | 1133 | 1145 | 1152 | 1174 | 1127 |
| $f_u$ (MPa) | 1210 | 1350 | 1359 | 1365 | 1373 | 1330 | 1185 | 1195 | 1235 | 1187 |
| $\varepsilon_{(0.2\%)}$ (%) | 0.72 | 0.81 | 0.81 | 0.81 | 0.82 | 0.81 | 0.70 | 0.70 | 0.72 | 0.71 |
| $\varepsilon_u$ (%) | 2.83 | 2.79 | 2.72 | 3.62 | 4.35 | 2.88 | 3.03 | 2.96 | 6.63 | 4.36 |
| $f_u/f_{(0.2\%)}$ | 1.04 | 1.22 | 1.21 | 1.22 | 1.20 | 1.17 | 1.03 | 1.04 | 1.05 | 1.05 |
| $\varepsilon_u/\varepsilon_{(0.2\%)}$ | 3.94 | 3.47 | 3.36 | 4.50 | 5.32 | 3.57 | 4.35 | 4.25 | 9.20 | 6.14 |
| Hardness (Hv) | 385 | 424 | 409 | 422 | 434 | 430 | 370 | 387 | 385 | 362 |
| $f_y$ P&V (MPa) | 1017 | 1129 | 1086 | 1123 | 1157 | 1146 | 973 | 1022 | 1017 | 950 |
| [a]$f_y$ (MPa) | 1073 | 1168 | 1131 | 1163 | 1192 | 1182 | 1037 | 1078 | 1073 | 1017 |
| $f_u$ P&V (MPa) | 1338 | 1483 | 1427 | 1476 | 1521 | 1506 | 1282 | 1345 | 1338 | 1252 |
| $f_u$ M (MPa) | 1232 | 1357 | 1309 | 1350 | 1389 | 1376 | 1184 | 1238 | 1232 | 1158 |
| [a]$f_u$ (MPa) | 1228 | 1350 | 1303 | 1344 | 1381 | 1369 | 1181 | 1234 | 1228 | 1156 |
| Charpy (J) | - | 112 | 128 | 128 | 128 | 125 | 96 | 96 | – | – |

*Refers to a standard size tensile test specimen.
[a] According to the current paper (Eqs. (4) & 5).

was considerably higher than that of measured in this paper. The fractured tensile test specimens are presented in Fig. 6.

## 4. Trends and relationships

The correlation between surface hardness and strength of each sub-zone was examined using available formulae proposed by Pavlina & Van Tyne [41], and Murakami [42] as presented in equations (1)–(3). For the sake of abbreviation, the former and latter were labelled with "P&V" and "M", respectively as shown in Tables 4 and 5 According to Pavlina & Van Tyne [41], the relationships between Vickers surface hardness (Hv) and yield ($f_y$)/ultimate strength ($f_u$) for the steels with yield strength between 300 and 1700 MPa as such:

$$f_y = (2.876Hv) - 90.7 \quad (1)$$

and,

$$f_u = (3.734Hv) - 99.8 \quad (2)$$

According to Murakami [42],

$$0.5f_u' = (1.6Hv) \pm 0.1Hv \quad (3)$$

in which it didn't provided a correlation between yield strength and surface hardness. Since the studied steel alloys didn't have a specific

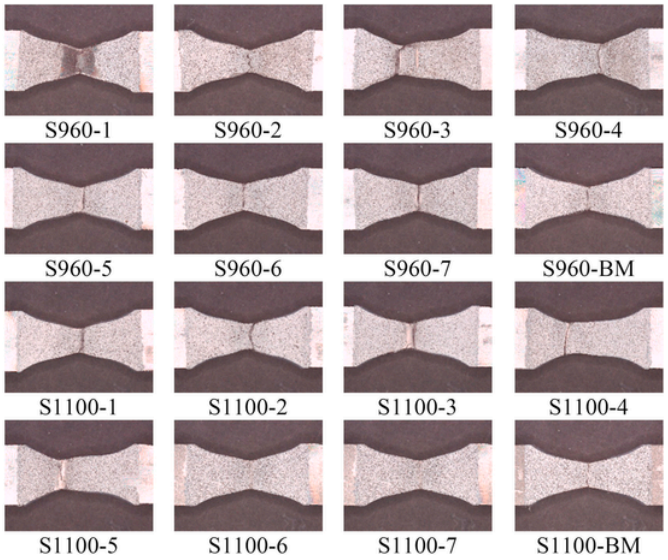


**Fig. 6.** Tensile test specimens after fracture (fracture location is visible from the painted area).

yield stress, the 0.2% proof stress was considered as equivalent yield stress in the proposed formulae.

Eq. (1) conservatively predicted the yield stress of S960 for all the simulated sub-zones, excluding specimen No. 4. It is notable that since this specimen failed from the softened zone outside the gauge area, the governed mechanical properties were not the actual values. For S1100 steel alloy, the prediction by Eq. (1) was matching well with sub-zones 1–5. However, for soft zones 6 and 7, it predicts 15% and 11% lower values, respectively.

Eq. (2) overestimated the $f_u$ of both steel alloys. Yet, the prediction for S960 was reasonably acceptable as the deviation was less than 5% in all sub-zones. However, the prediction of $f_u$ based on Eq. (2) for S1100 steel alloy was as high as 13% such as sub-zone 5.

Eq. (3) successfully predicted the $f_u$ for all sub-zones of the two steel alloys as shown in Tables 4 and 5, and Fig. 7. Hence, it is recommended to use this equation for the calculation of tensile strength in welded UHSS sub-zones. Even though this equation predicted the tensile properties of each sub-zone well, it can't be used for the calculation of the welded joint's strength such as the GMAW in this study. Due to the metallurgical constraint at the surrounding of the softened HAZ, higher strength was achieved in the welded joint.

It is notable that the data presented in Refs. [41,42] belonged to variety of steel alloys with different microstructure and chemical composition. The calculation errors assigned to equations (1)–(3) were due to the complexity of the microstructure of steels studied in this paper. Even though Pavlina & Van Tyne [41] tried to categorize the steels based on their microstructure, yet their proposal was generating inaccuracy which was due to the lack of enough data points (only 7 steels with complex microstructure were included). Since more data points were included in the current paper, it was tried to propose new formulae to correlate surface hardness and tensile strength in UHSSs with complex microstructure. Based on the available data, a least-squares linear regression analysis was performed, and the following equations were driven:

$$f_{(0.2\%)} = (2.432Hv) + 136.7 \quad (4)$$

$$f_u = (3.132Hv) + 22 \quad (5)$$

The validity range of the proposed equations was between 254 and 434 Hv. The coefficient of determination, $R^2$, of the above equations were, 0.8762 and 0.9815, respectively. It is notable that since sub-zone No. 4 of S960 failed from the softened region outside the gauge area, the data for this point was excluded in the regression analysis. The calculated 0.2% proof stress, and tensile strength of each replicated steel were presented in Tables 4 and 5 As can be seen from those tables, the 0.2% proof stress calculated according to Eq. (4) provided a better estimation compared to Eq. (1) specially for S960, as shown in Fig. 7. Hence, it is proposed to use this equation when dealing with steels with complex microstructure. The calculation of the $f_u$ based on Eq. (5) generated similar tensile strength compared Eq. (3) as can be seen in Fig. 7.

The Charpy impact toughness results are also presented in Tables 4 and 5 Since the specimens were sub-sized due to the thickness limitation of the BMs, a facture of two was multiplied to the original values as proposed by Afkhami et al. [17]. Fig. 8 shows the trend in Charpy impact toughness was like that of the hardness evaluation curve for both steel alloys. It was found that the softened HAZs in both steel alloys had also a lower impact toughness compared to the hardened specimens. The reason was behind the microstructure of the replicated HAZ specimens, phase fraction and grain size of each zone which is going to be explained in section 5.

## 5. Microstructural evaluation

The microstructure of S960 BM as presented in Fig. 9 was generally consisted of fine bainitic morphology as matrix which was placed within the elongated prior austenite grain. In addition, islands of martensite/austenite (M/A), partially/fully auto tempered martensite, and retained austenite were scattered throughout the bainitic matrix [29]. The whole microstructural constituents were also elongated in

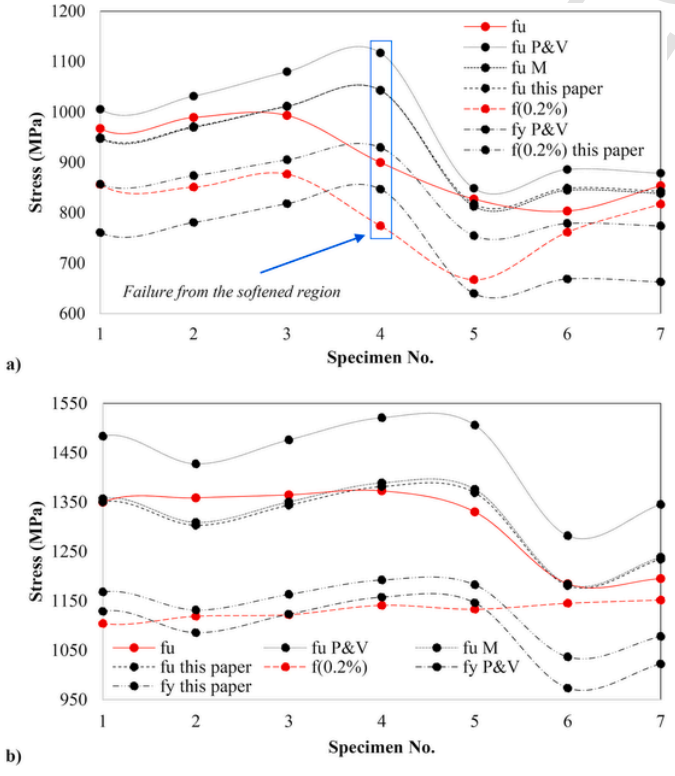


**Fig. 7.** Correlation between surface hardness and tensile strength, **a)** S960 and **b)** S1100.

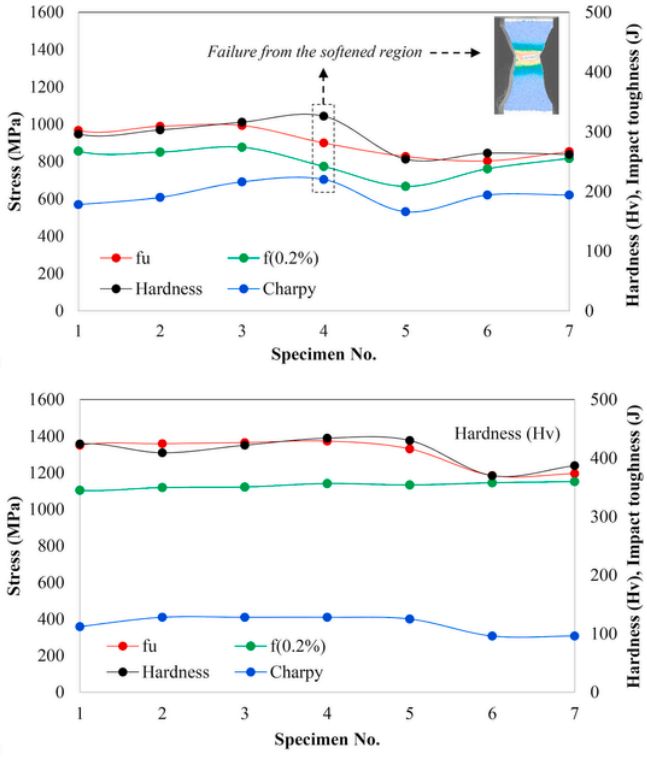


**Fig. 8.** The Mechanical properties specimens, **a)** S960 and **b)** S1100.

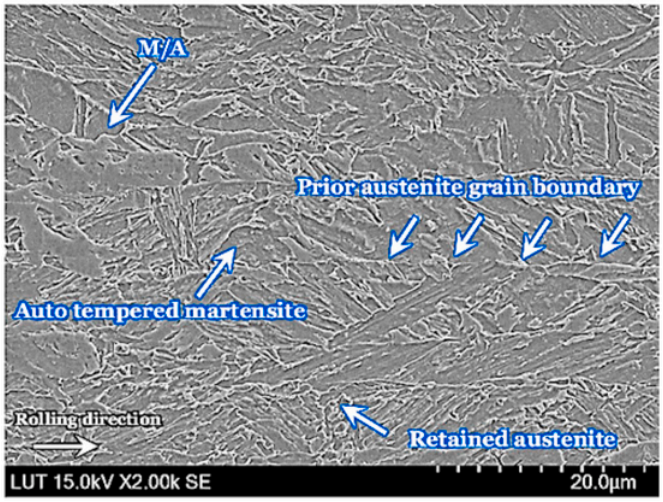


**Fig. 9.** The microstructure of S960 as the base metal [29].

the rolling direction due to the repetitive rolling-tempering treatment from the steel manufacturing process. As thoroughly discussed in Ref. [29], welding heat input has a significant impact on the microstructure of S960 and, consequently, its mechanical properties.

The microstructural features of the simulated sub-HAZs in S960 are presented in Fig. 10. Due to the welding HI, the elongated texture of the BM is eliminated in all the sub-zones and clear equiaxed grains are observed in Fig. 5(a-d). Moreover, a wide range of different phases with various distributions, sizes, and ratios is observed, depending on the distance from the weld FL. The difference is due to the unique thermal cycle that each region experienced during the welding (simulated) procedure, as shown in Fig. 1.

Depending on the distance from the FL, each sub-zone experienced a different peak temperature as shown in Table 3. By using Andrews' equation (Eq. (6)) [43], the austenitization finish temperature ($Ac_3$) of S960 is estimated at 855.4 °C. Hence, only specimens 1 to 4 experienced full austenitization during their heating and transformed back into a mixture of bainite and martensite while they were cooling down. As grain growth is a temperature-time dependent phenomenon, (prior) austenite grain size decreased gradually from 1 to 4 (specimen 1 had the highest peak temperature and the longest austenitization time, and vice versa). As an example, the boundaries of a single prior austenite grain are marked on Fig. 10(a). The gradual decrease in prior austenite grain size has resulted in a progressive increase in both 0.2% proof stress and tensile strength from the sub-zones 1 to 4. Even though the increase in the strength is not apparent in the sub-zone 4 (as the specimen failed from the softer region outside the gauge area), the strengthening effect can be observed in the ascending trend of the hardness values as shown in Fig. 4 (section 3).

$$Ac_3 = 910 - 203\times C_{wt\%}^{\frac{1}{2}} + 44.7\times Si_{wt\%} - 15.2\times Ni_{wt\%} + 31.5\times Mo_{wt\%} + 104.4\times V_{wt\%} + 13.1\times W_{wt\%} \quad \text{(Eq. 6)}$$

The sub-zone 5 were heated up to a two-phase region of $\alpha+\gamma$ as its peak temperature did not reach $Ac_3$, but exceeded the range of partial austenitization i.e. the peak temperature was between austenite start temperature ($Ac_1$) and $Ac_3$. As discussed in Ref. [29], the cooling rate in this region was not high enough to transform the partially austenitized microstructure to bainite or martensite. Therefore, it eventually transformed mainly into granular bainite (or polygonal ferrite) during the slow cooling time. Thus, the final microstructure (Fig. 10(e)) was a combination of granular bainite and tempered martensite, which resulted in decreasing 0.2% proof stress, tensile strength and hardness values. The lowest measured hardness in specimen 5 compared to other zones was expected to result in the highest notch (Charpy) fracture toughness. This is due to the inverse relationship between hardness and toughness. However, this sub-zone showed the lowest notch toughness among all S960 specimens. The controversy can be attributed to the formation of tempered martensite and ferrite which are usually associated with the formation of carbides.

In sub-zones 6 and 7, even though the peak temperature barely reached the austenitization start limit ($Ac_1$), they experienced temperature ranges high enough for tempering. Thus, through the heating stage, a portion of their primary microstructure transformed into tempered martensite and ferrite. Therefore, in comparison to the BM, 0.2% proof stress and tensile strength, as well as hardness values were decreased.

The microstructure of S1100 BM was also comprised a mixture of rough bainite accompanied by areas of M/A and small islands of retained austenite scattered around the mixture, as shown in Fig. 11 [17,29]. By using Eq. (6), $Ac_3$ of the BM is estimated at 857.4 °C, which is close to that of S960. However, in comparison to S960, S1100 has a significantly higher hardenability (CEV = 0.85% for S1100, in comparison to 0.59% for S960). Besides, S1100 is expected to have a lower and significantly smaller martensite start (Ms) and bainite start (Bs) temperatures, respectively. Calculated by Equations (7) and (8) [44], Ms and Bs temperatures for S1100 are estimated at 408.4 °C and 510.9 °C, respectively, which are lower than the equivalent values for S960 (468.5 °C and 633.7 °C, respectively).

$$B_s = 839 - \left(86\times Mn_{wt\%} + 23\times Si_{wt\%} + 67Cr_{wt\%} + 33\times Ni_{wt\%} + 75\times Mo_{wt\%}\right) - 270\times\left[1-\exp\left(-1.33\times C_{wt\%}\right)\right] \quad \text{(Eq. 7)}$$

$$M_s = 565 - \left(31\times Mn_{wt\%} + 13\times Si_{wt\%} + 10Cr_{wt\%} + 18\times Ni_{wt\%} + 12\times Mo_{wt\%}\right) - 600\times\left[1-\exp\left(-0.96\times C_{wt\%}\right)\right] \quad \text{(Eq. 8)}$$

Same as S960, the sub-zones of S1100 also revealed no elongated microstructure for the sub-zones crossed the austenitization limit, as shown in Fig. 12. For the sake of brevity, sub-zones with similar microstructural and mechanical features are presented as one image and only sub-zones 1, 3, 5, and 7 are shown. The sub-zones 1 to 4 were fully austenitized as the peak temperature during the heat up phase passing $Ac_3$. The fully austenitized microstructure was then transformed back into the mixture of bainite and martensite during the cooling phase. Microalloying elements seemingly prohibited the austenite from extensive grain growth (by comparing Figs 11(a) and 12(a). Besides, the high hardenability of the material resulted in transforming majority of the austenite into martensite and bainite. These simultaneous effects increased the tensile strength in zones 1–4 compared to the BM.

The sub-zone 5 experienced partial austenitization, same as S960-5. However, due to the high hardenability of S1100 and its low Ms and Bs temperatures, the austenite transformed back into a mixture of bainite and martensite. Hence, it prohibited this area from becoming a soft zone.

Regarding specimens 6 and 7 (Fig. 12(d)), since the peak temperature during the thermal cycle was below $Ac_1$, only tempering occurred. Consequently, a portion of the metastable martensite transformed into tempered martensite. Thus, the strength and hardness were deteriorated in these specimens compared to other zones. The tempered martensite also resulted in decreasing the notch fracture toughness of these two specimens.

## 6. Conclusions

The effects of weld thermal cycles on the mechanical properties and microstructure of the weld HAZ in two UHSS grades (i.e. S960 and

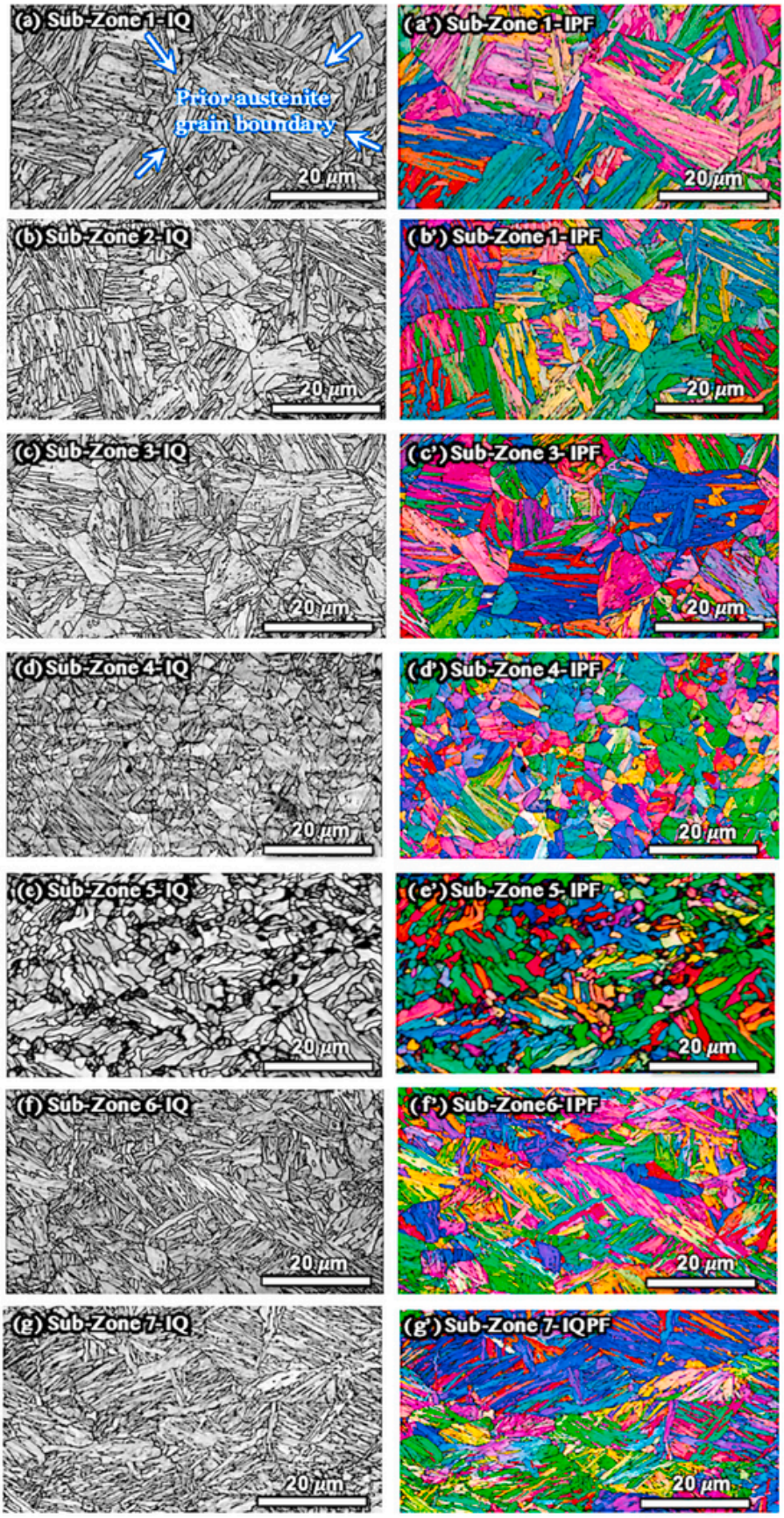
(a) Sub-Zone 1- IQ
Prior austenite grain boundary
20 μm
(a') Sub-Zone 1- IPF
20 μm
(b) Sub-Zone 2- IQ
20 μm
(b') Sub-Zone 1- IPF
20 μm
(c) Sub-Zone 3- IQ
20 μm
(c') Sub-Zone 3- IPF
20 μm
(d) Sub-Zone 4- IQ
20 μm
(d') Sub-Zone 4- IPF
20 μm
(e) Sub-Zone 5- IQ
20 μm
(e') Sub-Zone 5- IPF
20 μm
(f) Sub-Zone 6- IQ
20 μm
(f') Sub-Zone6- IPF
20 μm
(g) Sub-Zone 7- IQ
20 μm
(g') Sub-Zone 7- IQPF
20 μm

**Fig. 10.** The microstructural features of the sub-zones in S960 HAZ. (a) to (g) represent sub-zones 1–7 (closest to further from the FL), respectively. The left hand-side figures (a–g) are EBSD image quality (IQ) and right hand-side figures (a'-g') are EBSD inverse pole figures (IPF).

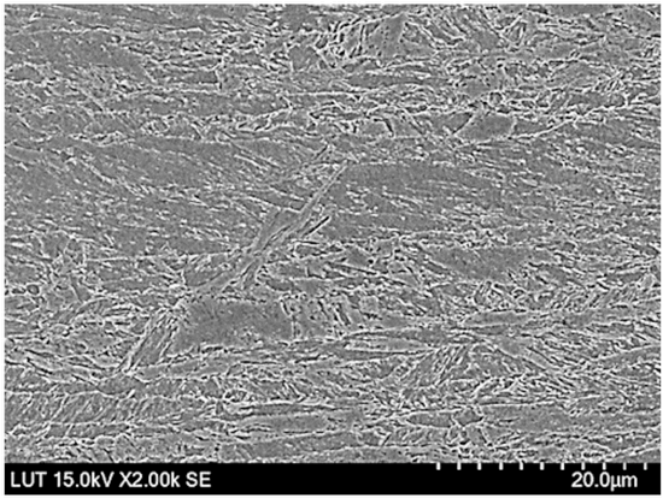


**Fig. 11.** The microstructure of S1100 BM [29].

S1100) was examined. For this aim, sub-sized specimens were simulated using a Gleeble 3800 thermal-mechanical simulator machine. The thermal cycles were representing the actual cycles of a GMAW with nominal HI value of 0.7 kJ/mm. Variety of characterization methods such as microhardness measurements, uniaxial tensile testing, Charpy impact toughness and microstructural analysis were implemented. According to the results, following conclusion were drawn:

- The surface hardness profiles of the sub-zones showed that the two steel alloys had different behavior under the weld thermal cycles. While the S960 suffered from severe softening at the ICHAZ with 29% hardness reduction, the maximum surface hardness reduction of the studied S1100 was only 4%. Also, a considerable hardening was observed at close distances to the FL in S1100 increasing the surface hardness up to 13%.
- The 0.2% proof stress and tensile strength of the studied HAZs followed the similar behavior as the surface hardness profiles. While the S960 lost 32% of its tensile strength at the sub-zone No. 5, the S1100 showed only 2% strength reduction at the sub-zone No. 6, followed by 13% increase at the sub-zone No. 4.
- Under the weld thermal cycles studied in this paper, both of the steel alloys showed an increase in their ductility ($\varepsilon_u/\varepsilon_{(0.2\%)}$) at the softened/hardened regions.
- Even though the two steel alloys show existence of a soft region in which tensile strength reduced, the overall strength of the joint was higher. Due to the metallurgical constraint at the HAZ caused by the surrounding material, higher tensile strength was achieved. Accordingly, while $f_u$ of S960 at sub-zone No. 5 showed 32% reduction, the welded joint's strength was 13% lower than the BM. Since the softened HAZ of S1100 had only 2% lower strength, with the presence of the boundary condition, strength of the joint raised above the BM and that the failure occurred at a far distance from the welded region.
- The applicability of available formula to correlate surface hardness of each sub-zone with $f_y/f_u$ proposed by Pavlina & Van Tyne [41], and Murakami [42] was examined. While Murakami's equation fairly predicted the $f_u$ of each sub-zone, using Pavlina & Van Tyne' equation to calculate strength of softened zones was inaccurate which was due to the microstructural complexity of the studied steels in this paper.
- An equation was proposed to correlate the Vickers surface hardness of steels with complex microstructure to $f_{(0.2\%)}$ and $f_u$ such that: $f_{(0.2\%)} = (2.432Hv) + 136.7$, and $f_u = (3.132Hv) + 22$.
- The BM of S960 had a fine bainitic microstructure accompanied with islands of M/A, tempered martensite, and retained austenite scattered around the bainitic matrix. During the welding procedure, the peak temperature was not high enough to fully austenitize the sub-zone No. 5. The partially austenitized material was not cooled down fast enough to transform into martensite and bainite. Thus, the final microstructure of this region included a considerable amount of tempered martensite which deteriorated the mechanical properties of this sub-zone (which is consequently recognized as softened HAZ).
- The microstructure of S1100 BM consisted of a mixture of rough bainite, M/A, and islands of retained austenite. Due to the higher hardenability of S1100, tempered martensite did not form in its partially austenitized sub-zone. However, tempering occurred in the sub-zones further from the fusion line (sub-zones 6 and 7) and resulted in the formation of tempered martensite. Therefore, the mechanical properties were relatively deteriorated in these sub-zones.

Further study is planned to elaborate the advanced microstructure characterization, including the fracture surfaces of tensile and impact samples.

## Author statement

Mohsen Amraei: Conceptualization; Data curation; Formal analysis; Investigation; Methodology; Software; Validation; Visualization; Roles/Writing - original draft; Writing - review & editing. Shahriar Afkhami: Conceptualization; Data curation; Formal analysis; Investigation; Methodology; Software; Roles/Writing - original draft; Writing - review & editing. Vahid Javaheri: Investigation (Microstructural Evaluation SEM/EBSD), Roles/Writing - original draft; Writing - review & editing. Jari Larkiola: Investigation (providing Gleeble facility); Methodology; Project administration. Tuomas Skriko: Conceptualization; Investigation (Tensile and Charpy Impact Toughness Tests). Timo Björk: Conceptualization; Funding acquisition; Investigation; Methodology; Project administration; Resources; Supervision; Validation. Xiao-Ling Zhao: Conceptualization; Funding acquisition; Investigation; Methodology; Project administration; Resources; Supervision; Validation; Writing - review & editing

## Declaration of competing interest

The authors declare that they have no known competing financial interests or personal relationships that could have appeared to influence the work reported in this paper.

## Acknowledgment

The authors would like to appreciate financial support of Business Finland through ISA-LUT project, and the Australian Research Council through a Discovery Project (DP150100442). The authors wish to thank SSAB Europe Co. by providing the steel plates for this research. Special thanks to the technical support of the staff members at Laboratory of Steel Structures, Laboratory of Welding Technology of LUT University. The help and support of Mr. Juha Uusitalo in performing the Gleeble simulations at the University of Oulu is highly appreciated.

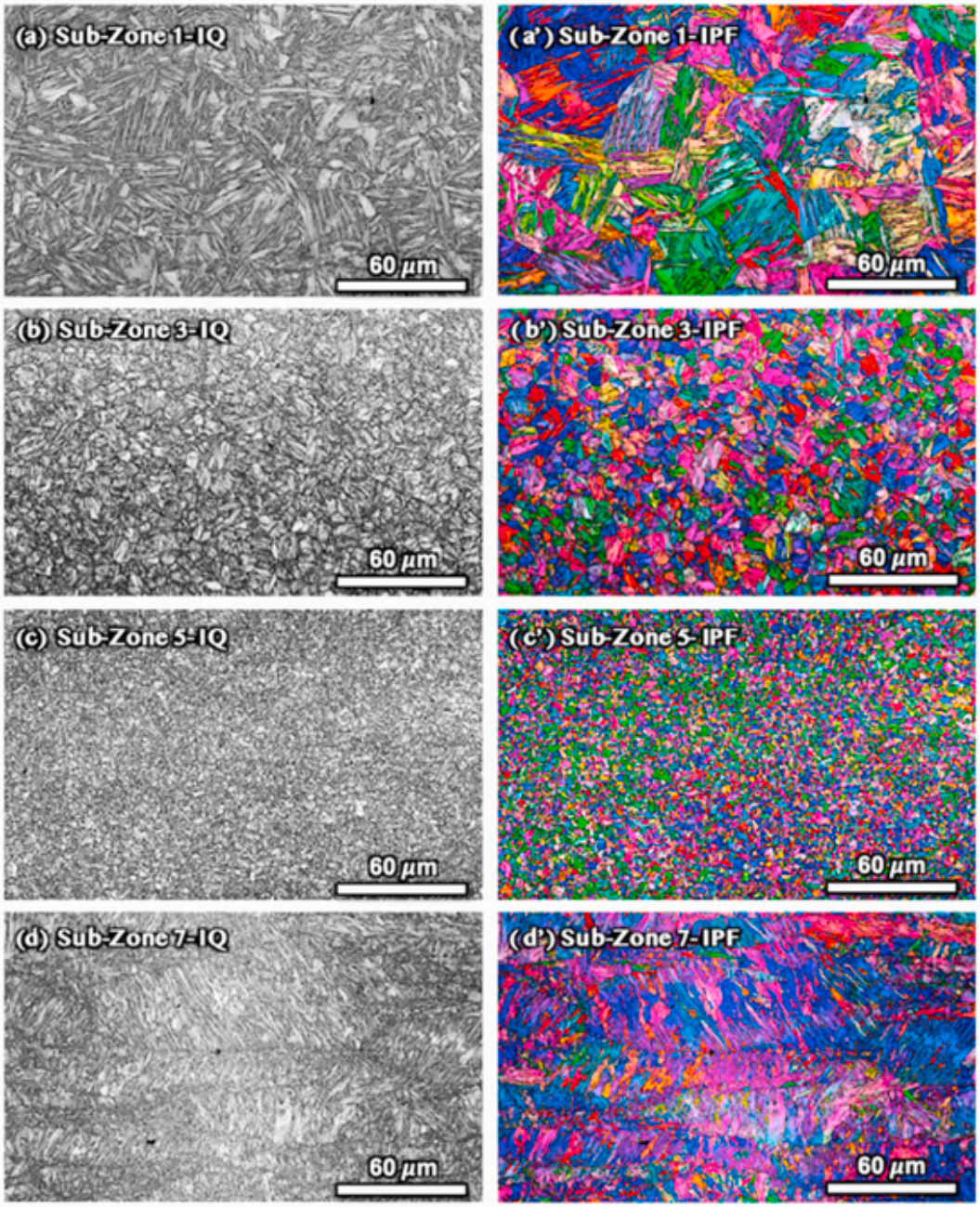


**Fig. 12.** The microstructural features of the sub-zones in S1100 HAZ. (a) to (d) represent sub-zones 1, 3, 5, and 7 (closest to further from the FL), respectively. The left hand-side figures (a–d) are EBSD image quality (IQ) and right hand-side figures (a'-d') are EBSD inverse pole figures (IPF).

## References


[1] R. Bjorhovde, Development and use of high performance steel, J. Constr. Steel Res. 60 (3) (2004) 393–400.

[2] X.-L. Zhao, A. Heidarpour, L. Gardner, Recent developments in high-strength and stainless steel tubular members and connections, Steel Construct. 7 (2) (2014) 65–72, doi:10.1002/stco.201410019.

[3] H. Ban, G. Shi, A review of research on high-strength steel structures, Struct. Build. 171 (8) (2018) 625–641.

[4] H.-T. Li, B. Young, Design of cold-formed high strength steel tubular sections undergoing web crippling, Thin-Walled Struct. 133 (2018) 192–205.

[5] L.-T. Hai, F.-F. Sun, C. Zhao, G.-Q. Li, Y.-B. Wang, Experimental cyclic behaviour and constitutive modelling of high strength structural steels, Construct. Build. Mater. 189 (2018) 1264–1285.

[6] S. Herion, O. Fleischer, R.J.M. Pijpers, C. Remde, B. Straetmans, Fatigue Behaviour of Hollow Sections Joints and High Strength Steel, CIDECT Report 7AB-3/19, CIDECT Annual Assembly, Barcelona, Spain, August 2019.

[7] X. Liu, K.-F. Chung, C.-H. Ho, M. Xiao, Z.-X. Huo, D.A. Nethercot, Mechanical behavior of high strength S690-QT steel welded sections with various heat input energy, Eng. Struct. 175 (2018) 245–256.

[8] S.P. Chiew C. Cheng M.S. Zhao C.K. Lee T.C. Fung Experimental study of welding effect on S690Q high strength steel butt jointsFirst published:16 Septemberhttps://doi.org/10.1002/cepa.11242019

[9] M. Nassirnia, A. Heidarpour, X.-L. Zhao, J. Minkkinen, Innovative hollow columns comprising corrugated plates and ultra high-strength steel tubes, Thin-Walled Struct. 101 (2016) 14–25.

[10] M. Farahi, A. Heidarpour, X.-L. Zhao, R. Al-Mahaidi, Parametric study on the static compressive behaviour of concrete-filled double-skin sections consisting of corrugated plates, Thin-Walled Struct. 107 (2016) 526–542.

[11] F. Javidan, A. Heidarpour, X.-L. Zhao, J. Minkkinen, Application of high strength and ultra-high strength steel tubes in long hybrid compressive members: experimental and numerical investigation, Thin-Walled Struct. 102 (2017) 273–285.

[12] H. Tervo, A. Kaijalainen, T. Pikkarainen, S. Mehtonen, D. Porter, Effect of impurity level and inclusions on the ductility and toughness of an ultra-high-strength steel, Mater. Sci. Eng. A 697 (2017) 184–193.

[13] X.-L. Zhao, Section capacity of very high strength (VHS) circular tubes under compression, Thin-Walled Struct. 37 (3) (2000) 223–240.
[14] M. Amraei, M. Dabiri, T. Björk, T. Skriko, Effects of workshop fabrication processes on the deformation capacity of S960 ultra-high strength steel, ASME J. Manuf. Sci. Eng. 138 (12) (2016).
[15] Y.H. Gao, S.Z. Liu, X.B. Hu, Q.Q. Ren, Y. Li, P. Dravid Vinayak, C.X. Wang, A novel low cost 2000 MPa grade ultra-high strength steel with balanced strength and toughness, Mater. Sci. Eng. A 759 (2019) 298–302.
[16] X.J. Zhang, Microhardness characterisation in developing high strength, high toughness and superior ballistic resistance low carbon Ni steel, Mater. Sci. Technol. 28 (2012) 818–822.
[17] S. Afkhami, T. Björk, J. Larkiola, Weldability of cold formed high strength and ultrahigh strength steels, J. Constr. Steel Res. 158 (2019) 86–98.
[18] D. Li, A. Paradowska, B. Uy, J. Wang, M. Khan, Residual stresses of box and I-shaped columns fabricated from S960 ultra-high-strength steel, J. Constr. Steel Res. 166 (2020) 105904.
[19] M. Nassirnia, A. Heidarpour, X.-L. Zhao, J. Minkkinen, Innovative hollow corrugated columns: a fundamental study, Eng. Struct. 94 (2015) 43–53.
[20] F. Javidan, A. Heidarpour, X.-L. Zhao, J. Minkkinen, Application of high strength and ultra-high strength steel tubes in long hybrid compressive members: experimental and numerical investigation, Thin-Walled Struct. 102 (2016) 273–285.
[21] W. Guo, L. Li, S. Dong, D. Crowther, A. Thompson, Comparison of microstructure and mechanical properties of ultra-narrow gap laser and gas-metal-arc welded S960 high strength steel, Optic Laser. Eng. 91 (2017) 1–15.
[22] M. Amraei, H. Jiao, X.-L. Zhao, L.-W. Tong, Fatigue testing of butt-welded high strength square hollow sections strengthened with CFRP, Thin-Walled Struct. 120 (2017) 260–268.
[23] F. Farrokhi, J. Siltanen, A. Salminen, Fiber laser welding of direct-quenched ultrahigh strength steels: evaluation of hardness tensile strength, and toughness properties at subzero temperatures, ASME J. Manuf. Sci. Eng. 137 (6) (2015).
[24] M. Amraei, T. Skriko, T. Björk, X.-L. Zhao, Plastic strain characteristics of butt-welded ultra-high strength steel (UHSS), Thin-Walled Struct. 109 (2016) 227–241.
[25] W. Guo, D. Crowther, J.A. Francis, A. Thompson, Z. Liu, L. Li, Microstructure and mechanical properties of laser welded S960 high strength steel, Mater. Des. 85 (2015) 534–548.
[26] J. Siltanen, T. Skriko, T. Björk, Effect of the welding process and filler material on the fatigue behavior of 960 MPa structural steel at a butt joint configuration, J. Laser Appl. 28 (2) (2016) 1–9.
[27] J.H. Lee, S.H. Park, H.S. Kwon, G.S. Kim, C.S. Lee, Laser, tungsten inert gas, and metal active gas welding of DP780 steel: comparison of hardness, tensile properties and fatigue resistance, Mater. Des. 64 (2014) 559–565, doi:10.1016/j.matdes.2014.0-7.065.
[28] M. St. Węglowski, M. Zeman, Prevention of cold cracking in ultra-high strength steel Weldox 1300, Arch. Civ. Mech. Eng. 14 (2014) 417–424.
[29] M. Amraei, A. Ahola, S. Afkhami, T. Björk, A. Heidarpour, X.-L. Zhao, Effects of heat input on the mechanical properties of butt-welded high and ultra-high strength steels, Eng. Struct. 198 (2019) 109460.
[30] K. Wallin, S. Pallaspuro, I. Valkonen, P. Karjalainen, P. Suikkanen, Fracture properties of high performance steels and their welds, Eng. Fract. Mech. 135 (2015) 219–231.
[31] S. Pallaspuro, H. Yu, A. Kisko, D. Porter, Z. Zhang, Fracture toughness of hydrogen charged as-quenched ultra-high-strength steels at low temperatures, Mater. Sci. Eng. A 688 (2017) 190–201.
[32] L.W. Tong, L.C. Niu, S. Jing, L.W. Ai, X.-L. Zhao, Low temperature impact toughness of high strength structural steel, Thin-Walled Struct. 132 (2018) 410–420.
[33] D.A. Porter, Weldable High-Strength Steels: Challenges and Engineering Applications. IIW International Conference High-Strength Materials - Challenges and Applications, Finland, Helsinki, July 2015, pp. 2–3.
[34] H.K.D.H. Bhadeshia, R.W.K. Honeycombe, Steels: Microstructure and Properties, 2006, pp. 223–229.
[35] H. Jiao, X.-L. Zhao, A. Lau, Hardness and compressive capacity of longitudinally welded very high strength steel tubes, J. Constr. Steel Res. 114 (2015) 405–416.
[36] E.J. Barrick, J.N. DuPont, Mechanical properties and microstructural characterization of simulated heat-affected zones in 10wt pct Ni steel, Mater. Sci. Eng. A 748 (2019) 189–204.
[37] G.R. Eisler, P.W. Fuerschbach, SOAR: an extensible suite of codes for weld analysis and optimal weld schedules, Proceedings of the Seventh International Conference Computer Technology Welding, NIST, San Fr. CA, 1997.
[38] P.W. Fuerschbach, G.R. Eisler, R.J. Steele, Weld procedure development with OSLW-Optimization software for laser welding, Proceedings of the Fifth International Conference Trends Weld, Res. Pine Mountian GA, 1998.
[39] ASTM E23-18, Standard Test Methods for Notched Bar Impact Testing of Metallic Materials, ASTM International, West Conshohocken, PA, 2018.
[40] H. Jiao, X.-L. Zhao, Adeline Lau, Hardness and compressive capacity of longitudinally welded very high strength steel tubes, J. Constr. Steel Res. 114 (2015) 405–416.
[41] E.J. Pavlina, C.J. Van Tyne, Correlation of yield strength and tensile strength with hardness for steels, J. Mater. Eng. Perform. 17 (1) (2008) 888–893.
[42] Y. Murakami, Metal Fatigue: Effects of Small Defects and Nonmetallic Inclusions, 1sted., Elsevier Science Ltd., Netherlands, 2002, p. 390.
[43] H. Kim, J. Inoue, M. Okada, K. Nagata, Prediction of Ac3 and martensite start temperatures by a data-driven model selection approach, ISIJ Int. 57 (12) (Dec. 2017) 2229–2236, doi:10.2355/isijinternational.ISIJINT-2017-212.
[44] S.M.C. Van Bohemen, Bainite and martensite start temperature calculated with exponential carbon dependence, Mater. Sci. Technol. 28 (4) (2012) 487–495.